On the distinct drag, reconfiguration and wake of perforated structures

Yaqing Jin[1]**, Jin-Tae Kim**[2]**, Shyuan Cheng**[2]**, Oumar Barry**[3]
and Leonardo P. Chamorro[2,4,5,]†

[1]Department of Mechanical Engineering, The University of Texas at Dallas, Richardson, TX 75080, USA

[2]Mechanical Science and Engineering Department, University of Illinois, Urbana, IL 61801, USA

[3]Department of Mechanical Engineering, Virginia Tech, Blacksburg, VA 24061, USA

[4]Civil and Environmental Engineering Department, University of Illinois, Urbana, IL 61801, USA

[5]Aerospace Engineering, University of Illinois, Urbana, IL 61801, USA

Using especially designed laboratory experiments, we demonstrate that the flow-driven deformation of sufficiently porous, wall-mounted, flexible plates can exhibit positive Vogel exponent V, i.e. drag proportional to the $(2 + V)$ power of the incoming flow velocity. High-resolution force balance, planar particle image velocimetry and particle tracking velocimetry are used to measure the drag force, flow characteristics and plate bending. For a flexible plate with relatively high porosity given by an array of regularly spaced square openings, we derive a simple analytical argument that accounts for the sub-quadratic trends of the drag in a range of flow velocities spanning one order of magnitude. There, the drag experienced by the structure is modulated by the contributions of the local structure containing an open area. The effective approach velocity for each of these sections appears to increase monotonically with increased structure deformation due to the reduced effect of local wakes produced by adjacent areas. The uncovered aerodynamic behaviour may help to understand the complex flow–structure interaction of perforated structures in nature and engineering.

Key words: flow–structure interactions

1. Introduction

Characterization of the flow-induced deformation of flexible structures has been the subject of intense research in the last decades due to its relevance in various engineering, biology and forestry fields (Taylor 1952; Daniel & Combes 2002; Harder *et al.* 2004; Vollsinger *et al.* 2005; Crawford & Platts 2008; Stanford *et al.* 2008; Vogel 2009). The reconfiguration of wall-mounted elastic structures under relative flow usually results in a reduction of the frontal area, and mean drag, D. The scaling $D \propto U_0^2$ of a rigid body may exhibit a relation $D \propto U_0^{2+V}$; here, U_0 is the incoming velocity and $V < 0$ is the so-called Vogel exponent (Vogel 1984, 1989).

† Email address for correspondence: lpchamo@illinois.edu

Evidence shows that $-4/3 < V < -0.1$, where the geometry and material of the structure, buoyancy, skin friction, incoming flow profile and other factors may affect this parameter (Vogel 1984; Alben, Shelley & Zhang 2002, 2004; Zhu & Peskin 2007; Zhu 2008; Gosselin, De Langre & Machado-Almeida 2010; Luhar & Nepf 2011; Leclercq & De Langre 2016; Bhati *et al.* 2018). Experimental works have shown that larger than quadratic drag laws are possible for systems with a ball covered by elastic round filament canopy (Gosselin & De Langre 2011) or inverted flags (Kim *et al.* 2013).

Porosity plays a significant role in natural structures; it modulates the aero- and hydrodynamic forces, the structure reconfiguration and the surrounding flow. Examples are ubiquitous; they range from coral groups (Tunnicliffe 1982), and insect wings (Santhanakrishnan *et al.* 2014) to dandelion seeds (Cummins *et al.* 2018). The variation of structure porosity influences the stream impinging its frontal surface, which either passes through the structure or circumvents it, significantly altering the velocity shear and therefore flow recirculation in the wake region. Early experiments by Castro (1971) pointed out that, for structures with Reynolds numbers in the range $2.5 \times 10^4 < Re < 9 \times 10^4$, a critical structure porosity exists where periodic Kármán vortex shedding can be triggered. The dependence between drag coefficient and porosity has been examined in various studies; pressure loss appears to be a function of the Reynolds number, *Re*, porosity ratio, β, and Mach number, *Ma* (Castro 1971; Koo & James 1973; Graham 1976; Laws & Livesey 1978). During the past decades, various studies have focused on establishing a robust model for predicting the drag coefficient as a function of porosity. Early efforts can be dated to Betz (1920), where potential flow was considered everywhere except regions very close to the structure; the model works well over a particular range of porosities, with underestimation of the drag coefficient at small porosities. An improved model was proposed by Koo & James (1973), which scaled the wake velocity to match the boundary conditions; experiments revealed underperformance in cases with low porosity. Recently, Steiros & Hultmark (2018) extended the model of Koo & James (1973) by including the influence of base suctions, leading to a much better prediction of drag at low porosity.

Most studies on perforated structures, however, have focused on rigid bodies. The role of porosity in the deformation and drag of flexible structures has not been explored in detail. Recently, Guttag *et al.* (2018) investigated the influence of base clamping on the static deformation of perforated plates; wake characteristics and direct measurements of drag were not explored. This work aims to contribute to the understanding of the dynamics of perforated, flexible plates; it focuses on the drag, wake and reconfiguration for various degrees of porosity, β. For the first time, we demonstrate that, over a critical porosity level, the Vogel exponent can be positive. This counter-intuitive phenomenon implies that flow-induced bending can lead to an increased drag coefficient. This distinct result offers new insight into the design of flexible structures subject to relative flow. The experimental set-up is described in § 2, the results are presented and discussed in § 3 and the main remarks are given in § 4.

2. Experimental set-up

We performed systematic experiments considering five flexible plates, which shared a length of $L = 300$ mm, width $b = 50$ mm, thickness $c = 1.2$ mm, Young's modulus $E = 3.72$ GPa and density $\rho_m = 1.12$ kg m^{-3}, but different porosity ratios. These structures were tested within the free-stream region of the Talbot wind tunnel at
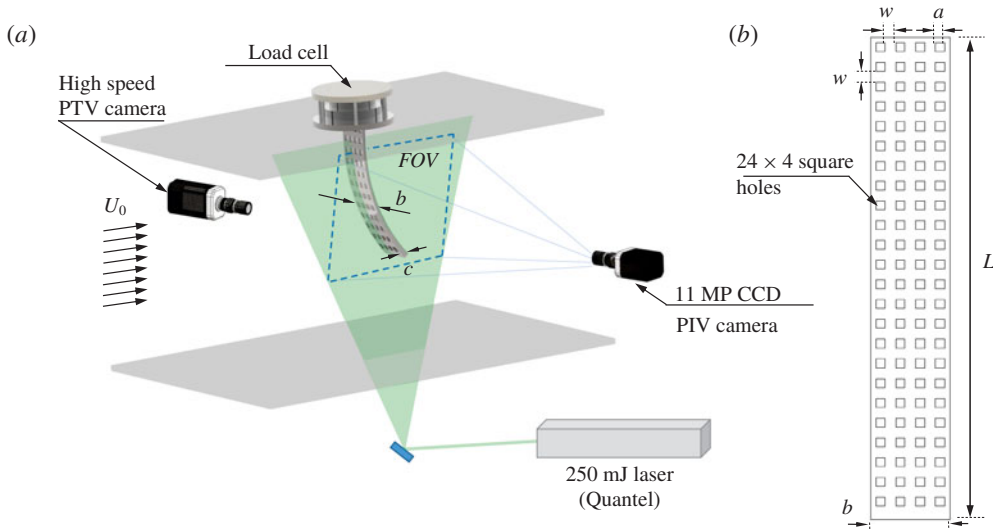
FIGURE 1. (*a*) Basic schematic of the experimental set-up illustrating the load cell, particle tracking velocimetry (PTV) and particle image velocimetry (PIV) systems; (*b*) general distribution of the porosity in a plate.

the University of Illinois (Adrian, Meinhart & Tomkins 2000), and mounted normal to the top wall as cantilever beams with the frontal area facing the incoming flow. There, the boundary layer effects were negligible (figure 1*a*). The ratio of the gravity force to the restoring force $G = \Delta\rho g b c L^3/(EI) = 0.66$ (Luhar & Nepf 2011), indicates that gravity plays a minor role in the plate deformation within the tested flow speeds. The porosity of the plates consisted of $N = 96$ square holes of side *a*, which were distributed uniformly along the span and width of the structures; this resulted in an array of 24×4 holes (see figure 1*b*). The selected levels of porosity were $\beta = [0, 0.5]$ every $\Delta\beta = 0.1$, which were controlled with the size of each square hole. For the selected β, $a = 0$, 3.95, 5.59, 6.85, 7.91 and 8.84 mm, and the space between holes was then $w = 12.5$, 8.55, 6.91, 5.65, 4.59 and 3.66 mm. It is worth noting that the equivalent mass per unit length ($\rho_m A_{eq}$) and equivalent bending stiffness (EI_{eq}) are determined by the plate porosity, which can be approximated as (Luschi & Pieri 2014; Barry & Tanbour 2018)

$$\left.\begin{aligned} \rho_m A_{eq} &= \frac{\rho_m bc(1 - N(\gamma - 2))\gamma}{N + \gamma}, \\ EI_{eq} &= EI \frac{(N + 1)\gamma(N^2 + 2N + \gamma^2)}{(1 - \gamma^2 + \gamma^3)N^3 + 3\gamma N^2 + (3 + 2\gamma - 3\gamma^2 + \gamma^3)\gamma^2 N + \gamma^3}, \end{aligned}\right\} \quad (2.1)$$

where $\gamma = w/[(w + a)]$. The large $L/b = 5$ and $L/c \gg 20$ suggest negligible influence of the Poisson ratio. However, porosity may influence the structural characteristics of the plates (Lee & Kim 2005; Barry & Tanbour 2018).

The aerodynamic force and deformation of each plate were characterized for 19 incoming velocities $U_0 \in [3.26, 11.54]$ m s^{-1} every $\Delta U_0 \approx 0.46$ m s^{-1}, resulting in Reynolds numbers of $Re = U_0 b/\nu \in [1.1, 3.8] \times 10^4$, where ν denotes the kinematic viscosity of air. Within the tested Re, complementary measurements show that the drag
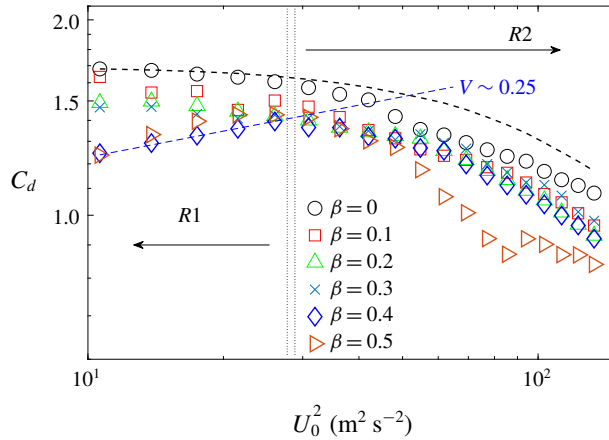
FIGURE 2. Distribution of the drag coefficient, C_d, as a function of incoming velocity, U_0, and structure porosity, β. The dashed black line denotes the trend for $\beta = 0$ following the relation by Luhar & Nepf (2011).

coefficient, C_d, of a rigid plate experience minor variations. The flexible plates were mounted on a high-resolution ATI Gamma load cell that measured instantaneous drag at a frequency of 1 kHz for periods of 30 s (Jin & Chamorro 2017; Jin *et al.* 2018*b*, 2019). All the forces were measured three times, 90 s each case. The uncertainty of the load cell in the worst scenario, i.e. under the minimum drag, was ~3%. A two-dimensional particle tracking velocimetry system was used to track fiducial points distributed along one side of each plate at a frequency of 300 Hz for periods of 30 s (Kim *et al.* 2016; Jin, Kim & Chamorro 2018*a*). A Halogen Spotlight illuminated the plates, and the motions were captured with a 2 MP high-speed camera. Flow in the vicinity of the plates was characterized by a PIV system from TSI. A wall-normal field of view of 350 mm × 280 mm crossing the centre of the plates was illuminated with a 1 mm thick laser sheet produced by a 250 mJ pulse^{-1} laser from Quantel. Two thousand image pairs were collected at 1 Hz by an 11 MP CCD camera, where the airflow was seeded with 1 μm olive oil particles. Images were interrogated with a recursive cross-correlation method with an interrogation window size of 16×16 pixels and 50% overlap, resulting in a vector grid spacing of $\Delta x = \Delta y = 0.9$ mm. To minimize any initial transient effect, the force fluctuations and tip motions were sampled after the steady state was reached (waiting time of at least 60 s).

3. Results

3.1. *On the drag coefficient*

Characterization of the drag and structure deformation of the various plates revealed distinct trends modulated by the degree of porosity. The time-averaged drag coefficient C_d of a perforated plate of porosity β, defined as

$$C_d = \frac{2D}{\rho_f U_0^2 bL(1-\beta)}, \tag{3.1}$$

where D is the time-averaged drag force, and ρ_f is the air density, is illustrated in figure 2. The base case with a non-perforated plate, i.e. $\beta = 0$, shows the C_d decreasing
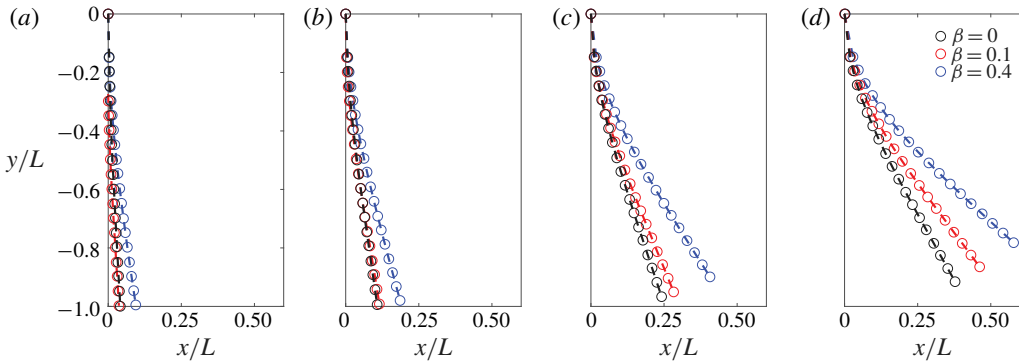
FIGURE 3. (*a–d*) Equilibrium plate deformation at $U_0 \approx 3.3$, 4.6, 7.4 and 10.2 m s^{-1}; the black, red and blue circles correspond to the $\beta = 0$, 0.1 and 0.4 plates.

monotonically with U_0 due to the increased structure deformation. Luhar & Nepf (2011) proposed a formulation for estimating C_d in these cases based on the plate bending along the span, as follows:

$$C_d \propto \int_0^L \cos^3 \theta \, \mathrm{d}s, \qquad (3.2)$$

where ds is the differential length along the plate span, and θ denotes the local bending angle. The estimation of C_d using (3.2) with direct PTV measurements of the plate reconfiguration is shown with the dashed black line. Overall, the trend fits reasonably well; some deviations are attributed to the tip effect. In general, the increase of β leads to lower C_d across U_0; some minor local exceptions may be attributed to experimental effects, and the coupled influence of plate reconfiguration and small recirculation regions induced by each perforation, which plays a central role in governing the drag distribution, as illustrated later. Except locally, C_d decreased with U_0 for $\beta \lesssim 0.3$; however, surprisingly, at sufficiently high values, namely $\beta = 0.4$ and 0.5, C_d exhibited an increase with U_0 in a low-velocity range (up to $U_0 \lesssim 5.1$ m s^{-1}, $R1$ in figure 2), which is followed by the expected decay as that with lower or no porosity plates ($R2$ in figure 2). Figure 3 illustrates the mean postures of the plates with $\beta = 0$, 0.1 and 0.4. Regardless of structure porosity, higher U_0 induced higher structure bending.

It is worth stressing that at $\beta = 0.4$ and 0.5 higher plate reconfiguration induced an increased drag coefficient for a range of comparatively low velocities. Specifically, $C_d \propto U_0^V$, where $V \geqslant 0.25$, i.e. the Vogel exponent of the mean drag is $V \geqslant 0.25$ (shown as dashed blue line in figure 2). Also note that, despite the observed significant bending for cases with $\beta = 0.4$ in figure 3, the corresponding C_d decreased less than the solid counterpart ($\approx 25\%$ compared to 36 % between $U_0 \approx 3.3$ and 11.5 m s^{-1}). This phenomenon indicates that the classical theory that provides the relation between flexible structure reconfiguration and drag is not applicable for structures with sufficiently high porosity.

3.2. *Wake characteristics induced by the bent perforated plates*

To explore the modulation of β by the drag and structure deformation, we characterized the flow field in the vicinity of the plates for the ranges of U_0 and β
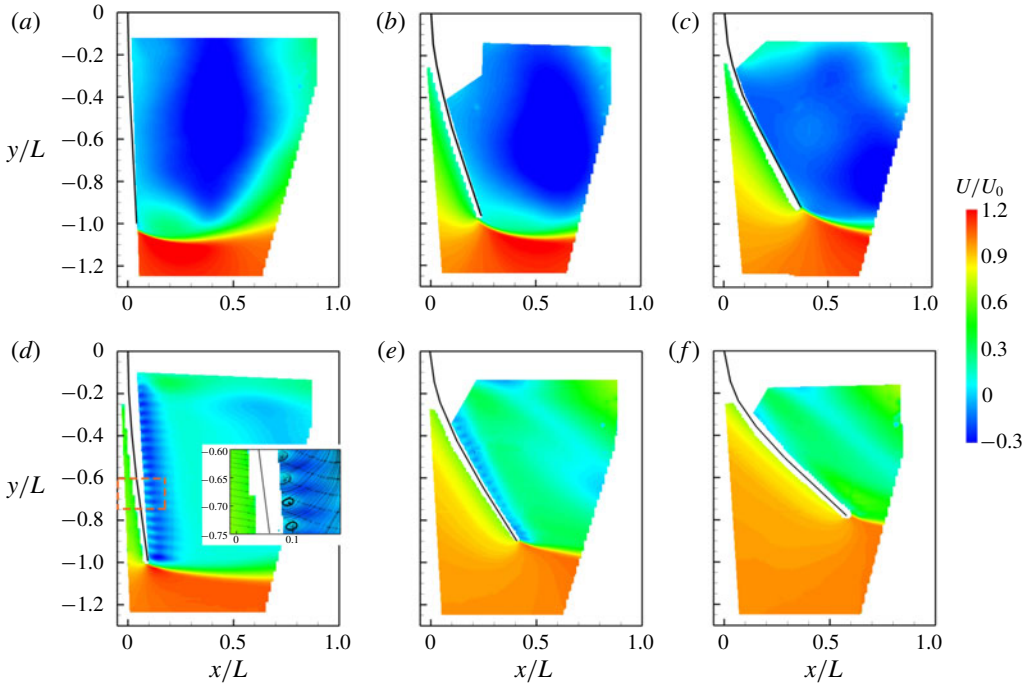
FIGURE 4. Time-averaged streamwise velocity distribution for plates with (a) $\beta = 0$, $U = 3.26$ m s^{-1}; (b) $\beta = 0$, $U = 7.4$ m s^{-1}; (c) $\beta = 0$, $U = 10.16$ m s^{-1}; (d) $\beta = 0.4$, $U = 3.26$ m s^{-1}; (e) $\beta = 0.4$, $U = 7.4$ m s^{-1}; (f) $\beta = 0.4$, $U = 10.16$ m s^{-1}. The inset in (d) superimposed with the streamlines highlights the local recirculation regions.

indicated above. Selected cases illustrating the time-averaged streamwise velocity distributions, U/U_0, are shown in figure 4. They reveal the distinctive impact of porosity in the very near wake region. The base structure (plate with no porosity) induced significant backward flow $U(x, y) \leqslant 0$ along the span with marked velocity excess near the tip across all U_0 (figure 4a–c). Due to the no-slip and no-penetration conditions, negligible flow occurred very close to the leeward surface of the plate. However, plate porosity altered the mean wake and flow near to the structure. Specifically, the region with backward flow reduced significantly due to the flow leakage through the plate, which facilitated the wake mixing and the velocity recovery (figure 4d–f). The location of the region with maximum velocity deficit shifted closer to the plate with high porosity; comparatively small backward flow regions appeared at regular intervals along the span of the structure. Such a phenomenon is particularly distinctive at small plate deformations, as highlighted in the inset of figure 4(d). There, superimposed streamlines show recirculation bubbles located between the backward flow areas, which matched with the square holes homogeneously distributed along the plate span. Figure 4 shows that the very near wake of the plate is composed of a series of small recirculation regions produced by the flow passing the open areas. The size of these recirculation bubbles is comparable to the width w (space between holes), which is approximately one order of magnitude smaller than b. The flow in the vicinity of the space between adjacent perforations appeared highly modulated by the neighbouring flow. Then, the drag on the plate can be thought of as the contribution of the drag produced by the flow passing through each rectangular grid
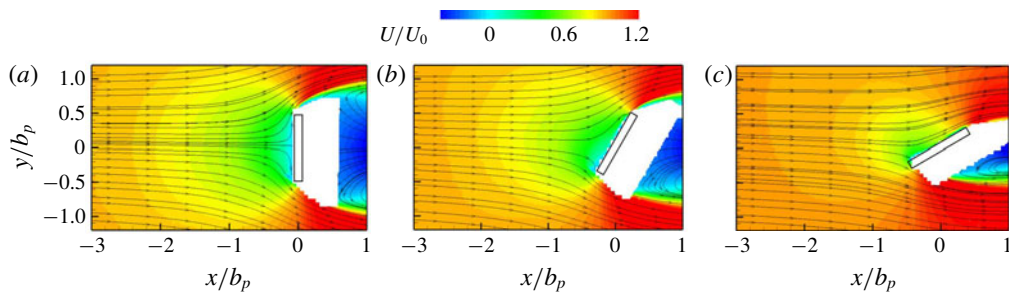
FIGURE 5. Time-averaged streamwise velocity distribution approaching a two-dimensional rigid plate with angles of attack of (*a*) 0°, (*b*) 30° and (*c*) 60°.

at sufficiently high porosity. Here, the local drag can be estimated with the local incoming velocity and local plate inclination.

Structures in the vicinity of others affect the flow, and the aerodynamic force (Ljungkrona, Norberg & Sunden 1991; Sumner *et al.* 1999; Sumner, Richards & Akosile 2005; Niu & Zhu 2006; Alam & Zhou 2013; Ma *et al.* 2017). The inclination of the plate dependent on the flow magnitude alters the flow dynamics in the vicinity of the space between adjacent perforations of thickness *w*. Estimation of the effective velocity impinging these sections along the plate span may provide a way to determine the bulk drag on the plate. It is important to note that the windward side of bluff bodies strongly influences the incoming flow in the vicinity of the structure (Hemmati, Wood & Martinuzzi 2016; Younis, Alam & Zhou 2016; Liu *et al.* 2017), which has to be accounted for in the estimation of the local (at scale *w*) and bulk (plate) drag. This phenomenon is inspected with complementary experiments using a two-dimensional rigid plate impinged by uniform flows under various angles of attack. There, regardless of the angle of attack, the incoming velocity at approximately $(2.5$–$3)b_p$ upwind of the structure, where b_p is the width of the rigid rectangular plate, is nearly the free stream (figure 5); it is an effective velocity, U_e, to compute the drag. Such a hint is, then, used to consider the effective velocity around each perforation of the plate, which was obtained via the time-averaged streamwise velocity distribution at $d = 2.5w$ upwind of the frontal plate surface.

3.3. *A basic model for the drag of highly perforated plates*

The distribution of U_e plays a key role in determining the drag force acting on flexible plates with high porosity. To quantify this influence, U_e of the $\beta = 0.4$ plate is shown in figure 6(*a*). As noted from the complementary experiments, the velocity profile at a distance of approximately $d = 2.5w$ upwind off the surface of the plate can be considered as the effective velocity around each perforation to calculate the local drag. Regardless, we inspected U at $d = 2.5$–$3.5w$ upwind of the plate surface as U_e in figure 6(*a*). Higher plate bending generates larger inclination angles in each section around a perforation, where the local wake induced weaker influence on the neighbouring perforation. This led to a monotonic increase of U_e with U_0. In the limiting case with the plate (surface vector) parallel to the incoming flow, $U_e = U_0$. Then, the relation between drag force acting on the structure (D_{model}) and U_e can be integrated as

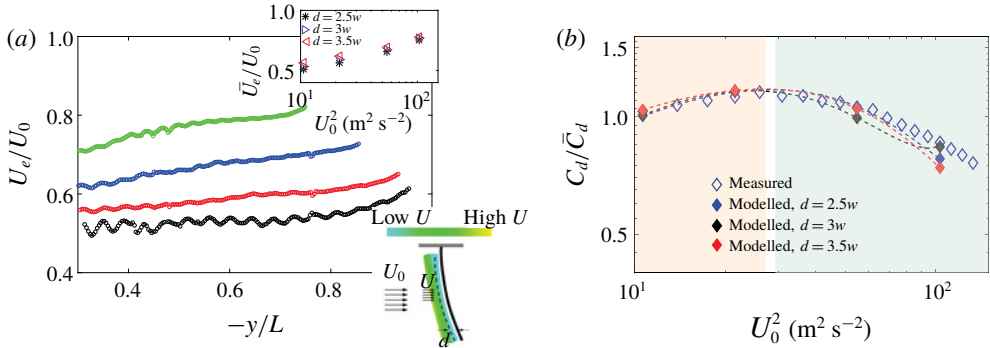$$D_{model} \propto \int_0^L \frac{1}{2} U_e^2 \cos^3 \theta \, ds. \tag{3.3}$$

FIGURE 6. (*a*) Distribution of the effective velocity U_e (obtained at $d = 2.5w$) along the $\beta = 0.4$ plate span at $U_0 = 3.26$ m s^{-1} (black), 4.64 m s^{-1} (red), 7.4 m s^{-1} (blue) and 10.16 m s^{-1} (green); the inset (top) shows the spatially averaged U_e for various upwind distances $2.5w$–$3.5w$, indicating negligible changes; the inset (bottom) shows a schematic of a time-averaged near field velocity distribution and locations where U_e is considered (dashed line, $d = 2.5w$–$3.5w$ upwind of the plate surface). (*b*) Comparison of measured and modelled $C_d/\bar{C}_d$ of the $\beta = 0.4$ plate for a range of velocities; the red and green dashed regions denote the range dominated by U_e (*R*1) and plate bending (*R*2).

Figure 6(*b*) illustrates the estimated and measured C_d normalized with its mean value $\bar{C}_d$ across U_0. The estimated C_d shows good agreement with the experimental results with $d \in [2.5, 3.5]w$. For relatively low U_0 ($U_0 \lesssim 5$ m s^{-1}, *R*1 marked red region), $dCd/dU_0 > 0$ may be affected by the increase of U_e, whereas for higher U_0 ($U_0 \gtrsim 6$ m s^{-1}, *R*2 marked green region), $dCd/dU_0 < 0$; there, the deformation of the plate modulates C_d, similar to the case of non-perforated plates.

As pointed out by Luhar & Nepf (2011), for an elastic, solid plate of sufficiently high aspect ratio, the drag may be determined by the extent of the structure bending or tip equilibrium location (X_{tip}) as

$$\left.\begin{array}{c} \dfrac{C_d(U_0)}{C_d(U_0 + \Delta U_0)} = \dfrac{\displaystyle\int_0^L \cos^3 \theta \, \mathrm{d}s|_{U_0}}{\displaystyle\int_0^L \cos^3 \theta \, \mathrm{d}s|_{U_0 + \Delta U_0}}, \\[1em] X_{tip} = \displaystyle\int_0^L \sin \theta \, \mathrm{d}s. \end{array}\right\} \quad (3.4)$$

So far, we have shown that this formulation cannot be extrapolated to perforated structures due to the significant effect of U_e. We introduce a non-dimensional parameter α in U_0 to further quantitatively evaluate the role of β in C_d over a range of flow velocities. Then, the drag coefficient can be written as

$$C_d = \frac{2D}{\rho_f(\alpha U_0)^2 bL(1 - \beta)}. \quad (3.5)$$

This way, α can be adjusted to match (3.4) for solid plates; its value provides a bulk quantification of the effect of porosity. The distribution of α for different plate porosities X_{tip} is shown in figure 7. For the base case with $\beta = 0$, $\alpha \approx 1$ remains
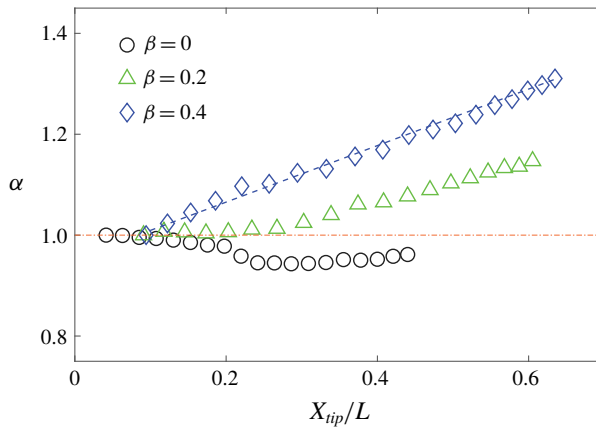
FIGURE 7. Non-dimensional parameter α as a function of tip equilibrium deformation X_{tip}/L and porosity, β.

approximately constant across all X_{tip}. The effect of porosity appears to be important at $\beta \gtrsim 0.1$; there, α increases monotonically with the plate tip bending due to the increase of U_e with U_0. At $\beta = 0.4$, α undergoes a significant, nearly linear increase with X_{tip} up to $\sim 30\%$ higher than its initial value, where the counter-intuitive, positive Vogel exponent occurred. Estimation of the effective velocity, or α, is not straightforward without direct measurement of the flow characteristics around the plate surface. As noted in figure 7, α increases monotonically with both X_{tip}/L and β. As a first-order approximation, a linear relationship can be defined as follows:

$$\alpha = A(\beta) + B X_{tip}/L, \tag{3.6}$$

where $A = A_0 + A_1 \beta$; in the inspected parameter space, $(A_0, A_1, B) \approx (0.9, 0.4, 0.3)$. Equation (3.6) provides a basic, first-order estimation of the effective velocity with a perforated, bent plate. It is worth stressing that it is based on cases with regularly spaced rectangular perforations. Inspection of the potential effect of perforation patterns and high-order formulation deserves particular attention.

4. Conclusions and remarks

In summary, our experiments examined the flow-induced deformation of wall-mounted perforated plates, their drag coefficient, structure bending and flow characteristics. We uncovered, for the first time, that structure bending may produce a higher drag coefficient, or equivalently, positive Vogel exponent, at sufficiently high structure porosity. To explain this phenomenon, we considered the bulk drag as the contribution of small regions containing a hole. We have demonstrated that the equivalent structure bending significantly alters the effective velocity, which may lead to the counter-intuitive trend of the drag coefficient. It is worth stressing that the effective velocity increases gradually from near the base of the plate to the tip, as noted in figure 6(*a*); this factor can be accounted for in the recent model by Guttag *et al.* (2018), which assumed a constant local drag coefficient over the extent of the strip. In addition, the distinct coupling between the effective velocity and equilibrium posture of the structure provides insight into the different drag coefficients of a given

perforated plate with different clamped configurations and, therefore, various postures, as reported in Guttag *et al.* (2018).

In this study, we have taken a step to quantitatively assess the complex fluid–structure interaction of perforated bodies with various degrees of porosity. There may be other parameters that deserve close inspection to obtain a full understanding of the reconfiguration of perforated structures. Geometry and distribution of the empty spaces (Castro 1971), the boundary conditions (Guttag *et al.* 2018) and even higher porosity may offer an unexpected relation between flow and drag. The uncovered positive Vogel exponent may be instrumental in explaining the complex dynamics of highly porous, flexible bodies in nature; examples range from canopies to wings.

Acknowledgements

Declaration of interests

The authors report no conflict of interest.

REFERENCES

ADRIAN, R. J., MEINHART, C. D. & TOMKINS, C. D. 2000 Vortex organization in the outer region of the turbulent boundary layer. *J. Fluid Mech.* **422**, 1–54.

ALAM, MD. M. & ZHOU, Y. 2013 Intrinsic features of flow around two side-by-side square cylinders. *Phys. Fluids* **25** (8), 085106.

ALBEN, S., SHELLEY, M. & ZHANG, J. 2002 Drag reduction through self-similar bending of a flexible body. *Nature* **420** (6915), 479–481.

ALBEN, S., SHELLEY, M. & ZHANG, J. 2004 How flexibility induces streamlining in a two-dimensional flow. *Phys. Fluids* **16** (5), 1694–1713.

BARRY, O. R. & TANBOUR, E. Y. 2018 Resonant frequencies of perforated plates with rectangular slots. *P I Mech. Engng C-J Mec.* **232** (7), 1247–1254.

BETZ, A. 1920 Das Maximum der theoretisch möglishen Ausnützung des Windes durch Windmotoren. *Zeitschr. Gesam. Turbinenw.* **26**, 307–309.

BHATI, A., SAWANNI, R., KULKARNI, K. & BHARDWAJ, R. 2018 Role of skin friction drag during flow-induced reconfiguration of a flexible thin plate. *J. Fluid Struct.* **77**, 134–150.

CASTRO, I. P. 1971 Wake characteristics of two-dimensional perforated plates normal to an air-stream. *J. Fluid Mech.* **46** (3), 599–609.

CRAWFORD, C. & PLATTS, J. 2008 Updating and optimization of a coning rotor concept. *J. Solar Energy Engng* **130** (3), 031002.

CUMMINS, C., SEALE, M., MACENTE, A., CERTINI, D., MASTROPAOLO, E., VIOLA, I. M. & NAKAYAMA, N. 2018 A separated vortex ring underlies the flight of the dandelion. *Nature* **562** (7727), 414.

DANIEL, T. L. & COMBES, S. A. 2002 Flexible wings and fins: bending by inertial or fluid-dynamic forces? *Integr. Compar. Biol.* **42** (5), 1044–1049.

GOSSELIN, F., DE LANGRE, E. & MACHADO-ALMEIDA, B. A. 2010 Drag reduction of flexible plates by reconfiguration. *J. Fluid Mech.* **650**, 319–341.

GOSSELIN, F. P. & DE LANGRE, E. 2011 Drag reduction by reconfiguration of a poroelastic system. *J. Fluid Struct.* **27** (7), 1111–1123.

GRAHAM, J. M. R. 1976 Turbulent flow past a porous plate. *J. Fluid Mech.* **73** (3), 565–591.

GUTTAG, M., KARIMI, H. H., FALCÓN, C. & REIS, P. M. 2018 Aeroelastic deformation of a perforated strip. *Phys. Rev. Fluids* **3** (1), 014003.

HARDER, D. L., SPECK, O., HURD, C. L. & SPECK, T. 2004 Reconfiguration as a prerequisite for survival in highly unstable flow-dominated habitats. *J. Plant Growth Regul.* **23** (2), 98–107.

HEMMATI, A., WOOD, D. H. & MARTINUZZI, R. J. 2016 Characteristics of distinct flow regimes in the wake of an infinite span normal thin flat plate. *Intl J. Heat Fluid Flow* **62**, 423–436.

JIN, Y. & CHAMORRO, L. P. 2017 Passive pitching of splitters in the trailing edge of elliptic cylinders. *J. Fluid Mech.* **826**, 363–375.

JIN, Y., KIM, J.-T. & CHAMORRO, L. P. 2018a Instability-driven frequency decoupling between structure dynamics and wake fluctuations. *Phys. Rev. Fluids* **3**, 044701.

JIN, Y., KIM, J.-T., FU, S. & CHAMORRO, L. P. 2019 Flow-induced motions of flexible plates: fluttering, twisting and orbital modes. *J. Fluid Mech.* **864**, 273–285.

JIN, Y., YAN, L., QIU, H. & CHAMORRO, L. P. 2018b Turbulence-driven reverse lift on two-dimensional and three-dimensional structures. *Phys. Rev.* E **98** (3), 033106.

KIM, D., COSSÉ, J., CERDEIRA, C. H. & GHARIB, M. 2013 Flapping dynamics of an inverted flag. *J. Fluid Mech.* **736**, R1.

KIM, J.-T., KIM, D., LIBERZON, A. & CHAMORRO, L. P. 2016 Three-dimensional particle tracking velocimetry for turbulence applications: case of a jet flow. *J. Vis. Exp.* **108**, e53745.

KOO, J.-K. & JAMES, D. F. 1973 Fluid flow around and through a screen. *J. Fluid Mech.* **60** (3), 513–538.

LAWS, E. M. & LIVESEY, J. L. 1978 Flow through screens. *Annu. Rev. Fluid Mech.* **10** (1), 247–266.

LECLERCQ, T. & DE LANGRE, E. 2016 Drag reduction by elastic reconfiguration of non-uniform beams in non-uniform flows. *J. Fluid Struct.* **60**, 114–129.

LEE, J.-K. & KIM, J.-G. 2005 An analytical study on prediction of effective elastic constants of perforated plate. *J. Mech. Sci. Technol.* **19** (12), 2224–2230.

LIU, B., HAMED, A. M., JIN, Y. & CHAMORRO, L. P. 2017 Influence of vortical structure impingement on the oscillation and rotation of flat plates. *J. Fluid Struct.* **70**, 417–427.

LJUNGKRONA, L., NORBERG, C. H. & SUNDEN, B. 1991 Free-stream turbulence and tube spacing effects on surface pressure fluctuations for two tubes in an in-line arrangement. *J. Fluid Struct.* **5** (6), 701–727.

LUHAR, M. & NEPF, H. M. 2011 Flow-induced reconfiguration of buoyant and flexible aquatic vegetation. *Limnol. Oceanogr.* **56** (6), 2003–2017.

LUSCHI, L. & PIERI, F. 2014 An analytical model for the determination of resonance frequencies of perforated beams. *J. Micromech. Microengng* **24** (5), 055004.

MA, S., KANG, C.-W., LIM, T.-B. A., WU, C.-H. & TUTTY, O. 2017 Wake of two side-by-side square cylinders at low Reynolds numbers. *Phys. Fluids* **29** (3), 033604.

NIU, J. & ZHU, Z. 2006 Numerical study of three-dimensional flows around two identical square cylinders in staggered arrangements. *Phys. Fluids* **18** (4), 044106.

SANTHANAKRISHNAN, A., ROBINSON, A. K., JONES, S., LOW, A. A., GADI, S., HEDRICK, T. L. & MILLER, L. A. 2014 Clap and fling mechanism with interacting porous wings in tiny insect flight. *J. Expl Biol.* **217** (21), 3898–3909.

STANFORD, B., IFJU, P., ALBERTANI, R. & SHYY, W. 2008 Fixed membrane wings for micro air vehicles: experimental characterization, numerical modeling, and tailoring. *Prog. Aerosp. Sci.* **44** (4), 258–294.

STEIROS, K. & HULTMARK, M. 2018 Drag on flat plates of arbitrary porosity. *J. Fluid Mech.* **853**, R3.

SUMNER, D., RICHARDS, M. D. & AKOSILE, O. O. 2005 Two staggered circular cylinders of equal diameter in cross-flow. *J. Fluid Struct.* **20** (2), 255–276.

SUMNER, D., WONG, S. S. T., PRICE, S. J. & PAIDOUSSIS, M. P. 1999 Fluid behaviour of side-by-side circular cylinders in steady cross-flow. *J. Fluid Struct.* **13** (3), 309–338.

TAYLOR, G. I. 1952 Analysis of the swimming of long and narrow animals. *Proc. R. Soc. Lond.* A **214** (1117), 158–183.

TUNNICLIFFE, V. 1982 The effects of wave-induced flow on a reef coral. *J. Exp. Mar. Biol. Ecol.* **64** (1), 1–10.

VOGEL, S. 1984 Drag and flexibility in sessile organisms. *Am. Zool.* **24** (1), 37–44.

VOGEL, S. 1989 Drag and reconfiguration of broad leaves in high winds. *J. Expl Bot.* **40** (8), 941–948.

VOGEL, S. 2009 Leaves in the lowest and highest winds: temperature, force and shape. *New Phytol.* **183** (1), 13–26.

VOLLSINGER, S., MITCHELL, S. J., BYRNE, K. E., NOVAK, M. D. & RUDNICKI, M. 2005 Wind tunnel measurements of crown streamlining and drag relationships for several hardwood species. *Can. J. Forest Res.* **35** (5), 1238–1249.

YOUNIS, M. Y., ALAM, M. M. & ZHOU, Y. 2016 Flow around two non-parallel tandem cylinders. *Phys. Fluids* **28** (12), 125106.

ZHU, L. 2008 Scaling laws for drag of a compliant body in an incompressible viscous flow. *J. Fluid Mech.* **607**, 387–400.

ZHU, L. & PESKIN, C. S. 2007 Drag of a flexible fiber in a 2D moving viscous fluid. *Comput. Fluids* **36** (2), 398–406.